

Magnetohydrodynamic flow in precessing spherical shells

By A. TILGNER

Institute of Physics, University of Bayreuth, D-95440 Bayreuth, Germany

(Received 26 August 1997 and in revised form 26 August 1998)

Flow in a rapidly rotating, precessing spherical shell is studied with and without an applied magnetic dipole field in order to model the Earth's core. The primary response of the fluid to precessional forcing is a solid body rotation about an axis other than the rotation axis of the shell. The orientation and energy of that flow is predicted well by an asymptotic theory. Ekman layers at the boundaries of the shell break down at critical latitudes and spawn internal shear layers. The limit of small precession rate is investigated in particular: at zero magnetic field, the strongest shear layers are inclined at 30° with respect to the rotation axis of the shell and erupt at 30° latitude from the inner core. When a magnetic dipole field with its dipole oriented along the rotation axis of the shell is applied, shear zones develop additional structure and change position and orientation. At an Elsasser number of 10, most flow structures tend to align with the rotation axis of the shell.

1. Introduction

It is generally accepted that the origin of the geomagnetic field is a dynamo effect acting in the electrically conducting fluid in the outer core of the Earth. The driving mechanism for this flow is commonly believed to be convection, either thermal or compositional. Bullard (1949) first discussed the Earth's precession as an alternative driving force. The energy stored in the precessional motion of the Earth is sufficient to maintain the geomagnetic field for a long time. It is however unclear whether a mechanism exists by which this energy can be fed into fluid motion suitable for the dynamo effect. Kerswell (1996) has derived upper bounds for the energy dissipation in precessional flows which indicate that enough energy can be transferred from the precessing mantle to the fluid core in order to meet the energy requirements of the geodynamo.

Apart from the geophysical application, precession-driven flows have also received attention from the engineering community working on the dynamics of spinning spacecrafts containing liquid fuel (Vanyo & Likins 1972).

This paper treats flows with and without an imposed magnetic dipole field in precessing spherical shells as a model for the fluid motion in the Earth's core. Two major simplifications are made in going from the Earth's core to the model used here. First, it is assumed that the temperature gradient in the core is adiabatic so that neither convection nor stable stratification have any influence. Second, the ellipticity of the core is not taken into account. Pressure forces in addition to viscous friction couple the fluid to the motion of oblate boundaries. Only viscous forces are available to transmit the movement of spherical boundaries to the fluid. Irrespective of the precise form of the container, the Ekman layers break down at 'critical' latitudes and

spawn internal shear layers. These singularities occur at latitudes of $\pm 30^\circ$ in a sphere (Bondi & Lyttleton 1953; Stewartson & Roberts 1963; Kerswell 1995). Internal shear layers are a possible source of instability for the flow, but other instability mechanisms exist in an ellipsoidal casing. The geometry of a spherical shell therefore offers the opportunity to study viscous effects in isolation.

A series of experiments has investigated the structure of precession-driven flows in spheroids without an inner core (Malkus 1968; Vanyo *et al.* 1995). The flow consists mainly of a constant-vorticity flow with a vorticity vector which deviates from the rotation axis of the casing. Superimposed on this constant-vorticity flow is a number of nested cylindrical shear layers with axes roughly parallel with the rotation axis of the fluid. These shear layers become unstable and the flow eventually becomes turbulent if the precession rate is large enough. Gans (1970) has built a precessing cylinder filled with liquid sodium. The experiment was too small to operate as a dynamo, but an applied magnetic field was amplified by factors of up to 3.

Theoretical work has been concerned with viscous corrections to a basic constant-vorticity flow which is a solution of the inviscid problem. Stewartson & Roberts (1963), Roberts & Stewartson (1965) and Busse (1968) treat the case of small Ekman and Rossby numbers and deduce the orientation and angular velocity of that primary flow. In addition, Busse (1968) provides a description of the axisymmetric shear layer which is due to non-linearities in the boundary layers at the critical latitudes. Experiments have shown that while the shear layer considered by Busse is the strongest, others exist. Vanyo & Likins (1972) also propose a formula for the orientation and angular velocity of the primary flow based on empirical estimates of the frictional force exerted through the Ekman layer on the interior fluid. Hollerbach & Kerswell (1995) study the spin-over mode which is excited when the rotation axis of a spherical shell is impulsively tipped and the resulting flow left to decay. Shear layers due to singularities in the Ekman layers have been observed numerically. The numerical results have been consistent with the analytical work of Kerswell (1995). The nonlinear response induced by these shear layers, which are inclined at the characteristic angle of 30° with respect to the axis of rotation, has been shown to give rise to axisymmetric shear layers, decaying in time, akin to the structures visualized in experiments.

The present paper deals with the forced (as opposed to decaying) flow in a precessing spherical shell with an inner core. An inner core has been missing in the experiments and will be shown to largely dictate the structure of the flow. There is no attempt to treat instabilities or the dynamo effect, but as a preliminary step the influence of an imposed magnetic dipole field is studied. The numerical work is divided into two steps. First, a direct simulation allows quantities not easily accessible in experiments (§3) to be extracted. In order to unravel the dynamics and reduce the computational burden, a perturbation approach valid in the limit of small precession rates is adopted in a second step (§§4 and 5). Only within this framework has it been practical to include magnetic fields. Modifications of the shear layers due to magnetic effects are investigated. Conclusions will be drawn in the last section.

2. Mathematical formulation of the problem and numerical methods

We consider a fluid of density ρ , kinematic viscosity ν , and conductivity σ in a spherical shell of gap width d rotating with angular frequency ω . Units of length, time and magnetic field strength are chosen as d , $1/\omega$ and $(\rho\mu_0)^{1/2}d\omega$, respectively, with μ_0 the vacuum magnetic permeability. The non-dimensional equations for the velocity \mathbf{u} and magnetic field \mathbf{B} then read, in a frame of reference attached to the precessing

sphere (hereafter called the 'mantle system'),

$$\frac{\partial}{\partial t} \mathbf{u} + (\nabla \times \mathbf{u}) \times \mathbf{u} + 2(\hat{\mathbf{z}} + \boldsymbol{\Omega}) \times \mathbf{u} = -\nabla \Phi + Ek \nabla^2 \mathbf{u} - (\boldsymbol{\Omega} \times \hat{\mathbf{z}}) \times \mathbf{r} + (\nabla \times \mathbf{B}) \times \mathbf{B}, \quad (1)$$

$$\frac{\partial}{\partial t} \mathbf{B} + \nabla \times (\mathbf{B} \times \mathbf{u}) = \frac{Ek}{Pm} \nabla^2 \mathbf{B}. \quad (2)$$

Hats denote unit vectors. The Ekman number Ek and the magnetic Prandtl number Pm are given by $Ek = \nu/d^2\omega$ and $Pm = \mu_0\sigma\nu$. Φ stands for a reduced pressure which is immaterial in what follows because only the curl of (1) will be used. The rotation of the shell is in the z -direction and $\boldsymbol{\Omega}$ is the precession vector. The precession axis $\hat{\boldsymbol{\Omega}}$ forms an angle α ($0 < \alpha < \frac{1}{2}\pi$) with the z -axis and is time dependent in the mantle system:

$$\hat{\boldsymbol{\Omega}} = \sin \alpha \cos t \hat{\mathbf{x}} - \sin \alpha \sin t \hat{\mathbf{y}} + \cos \alpha \hat{\mathbf{z}}. \quad (3)$$

Retrograde precession corresponds to $\Omega < 0$. The magnetic field considered in this work is composed of an applied dipole field \mathbf{B}_d with the dipole oriented along the z -axis and an induced magnetic field \mathbf{b} , $\mathbf{B} = \mathbf{B}_d + \mathbf{b}$. The dipole field is given by

$$\mathbf{B}_d = (El Ek/Pm)^{1/2} (r_i r_o/r^2)^{3/2} (2 \cos \theta \hat{\mathbf{r}} + \sin \theta \hat{\boldsymbol{\theta}}) \quad (4)$$

in spherical polar coordinates (r, θ, φ) with El the Elsasser number. Normalization is such that $\frac{1}{2} \int (\mathbf{B}_d^2 + \mathbf{B}_{d\theta}^2) dV/V = El Ek/Pm$, where the integral extends over the volume V of the shell. r_i and r_o denote the inner and outer radii of the shell. Throughout this paper, $r_o - r_i = 1$ and $r_i/r_o = 0.35$ as appropriate for the Earth's core.

The boundary conditions require that $\mathbf{u} = 0$ at $r = r_i, r_o$ and that \mathbf{B} matches a vacuum field at the inner and outer boundaries. The assumption that the inner core is a vacuum is of course contrary to geophysical fact. But simulations with these boundary conditions allow the differences between the convex inner and concave outer boundary to be discerned, which are quite important even in the non-magnetic case (Kerswell 1995).

The solenoidal fields can be written in terms of poloidal and toroidal scalars

$$\mathbf{u} = \nabla \times \nabla \times (v\hat{\mathbf{r}}) + \nabla \times (w\hat{\boldsymbol{\theta}}), \quad \mathbf{b} = \nabla \times \nabla \times (g\hat{\mathbf{r}}) + \nabla \times (h\hat{\boldsymbol{\theta}}), \quad (5)$$

which are themselves decomposed into radial and angular parts:

$$\left. \begin{aligned} v &= r \sum_{l=1}^{\infty} \sum_{m=-l}^l V_l^m(r, t) P_l^m(\cos \theta) e^{im\varphi}, & w &= r^2 \sum_{l=1}^{\infty} \sum_{m=-l}^l W_l^m(r, t) P_l^m(\cos \theta) e^{im\varphi}, \\ g &= \sum_{l=1}^{\infty} \sum_{m=-l}^l G_l^m(r, t) P_l^m(\cos \theta) e^{im\varphi}, & h &= \sum_{l=1}^{\infty} \sum_{m=-l}^l H_l^m(r, t) P_l^m(\cos \theta) e^{im\varphi}, \end{aligned} \right\} \quad (6)$$

where $P_l^m(\cos \theta)$ denotes associated Legendre functions. Operating with $\hat{\mathbf{r}} \cdot \nabla \times$ and $\hat{\mathbf{r}} \cdot \nabla \times \nabla \times$ on (1) and with $\hat{\mathbf{r}} \cdot \nabla \times$ and $\hat{\mathbf{r}} \cdot \nabla \times \nabla \times$ on (2) one obtains

$$\frac{\partial}{\partial t} D_l V_l^m - Ek D_l^2 V_l^m = \frac{r}{l(l+1)} [\hat{\mathbf{r}} \cdot \nabla \times \nabla \times \{ \boldsymbol{\Omega}' \times \mathbf{u} - (\nabla \times \mathbf{b}) \times (\mathbf{B}_d + \mathbf{b}) \}]_l^m, \quad (7a)$$

$$\begin{aligned} \frac{\partial}{\partial t} W_l^m - Ek \left(\frac{\partial^2}{\partial r^2} + \frac{4}{r} \frac{\partial}{\partial r} + \frac{2-l(l+1)}{r^2} \right) W_l^m \\ = -\frac{1}{l(l+1)} [\hat{\mathbf{r}} \cdot \nabla \times \{ \boldsymbol{\Omega}' \times \mathbf{u} - (\nabla \times \mathbf{b}) \times (\mathbf{B}_d + \mathbf{b}) \}]_l^m + [f]_l^m, \end{aligned} \quad (7b)$$

$$\frac{\partial}{\partial t} G_l^m - \frac{Ek}{Pm} \left(\frac{\partial^2}{\partial r^2} - \frac{l(l+1)}{r^2} \right) G_l^m = -\frac{r^2}{l(l+1)} [\hat{\mathbf{r}} \cdot \nabla \times \{(\mathbf{B}_d + \mathbf{b}) \times \mathbf{u}\}]_l^m, \quad (7c)$$

$$\frac{\partial}{\partial t} H_l^m - \frac{Ek}{Pm} \left(\frac{\partial^2}{\partial r^2} - \frac{l(l+1)}{r^2} \right) H_l^m = -\frac{r^2}{l(l+1)} [\hat{\mathbf{r}} \cdot \nabla \times \nabla \times \{(\mathbf{B}_d + \mathbf{b}) \times \mathbf{u}\}]_l^m, \quad (7d)$$

with

$$\boldsymbol{\Omega}' = \nabla \times \mathbf{u} + 2(\hat{\mathbf{z}} + \boldsymbol{\Omega}), \quad D_l = \frac{\partial^2}{\partial r^2} + \frac{2}{r} \frac{\partial}{\partial r} - \frac{l(l+1)}{r^2}, \quad f = \Omega \sin \alpha [iP_1^l e^{i(\varphi+t)} + 2iP_1^{l-1} e^{-i(\varphi+t)}].$$

$[]_l^m$ denotes the l, m -component of the quantity in the square bracket. These equations need to be solved subject to the boundary conditions

$$V_l^m = \frac{\partial V_l^m}{\partial r} = W_l^m = 0 \quad \text{at} \quad r = r_i, r_o, \quad (8a)$$

$$H_l^m = \left(\frac{\partial}{\partial r} - \frac{l+1}{r_i} \right) G_l^m = 0 \quad \text{at} \quad r = r_i, \quad H_l^m = \left(\frac{\partial}{\partial r} + \frac{l}{r_o} \right) G_l^m = 0 \quad \text{at} \quad r = r_o. \quad (8b)$$

The detailed structure of the numerical code used in this work need not be elaborated here since it has evolved from a program previously used and extensively tested for the simulation of thermal convection (Tilgner 1996; Tilgner & Busse 1997) and the kinematic dynamo problem (Tilgner 1997). For additional validation, the decay rates obtained with a direct eigenvalue method by Hollerbach & Kerswell (1995) have been reproduced with the time integration method to within a few 10^{-3} . The code is a pseudo-spectral method which uses Chebychev collocation in the radial direction to complete the spatial discretization of the original equations and all nonlinear products are computed in direct space. The only difference with respect to previous versions resides in the time step. The nonlinear terms, the diffusion terms and the forcing f are treated with second-order Adams–Bashforth, implicit Euler and Crank–Nicholson steps, respectively. The rationale behind this time step and issues of resolution will be discussed in a separate publication (Tilgner 1999).

The direct simulations described in the next section required resolutions of up to 129 Chebychev polynomials and spherical harmonics of degree up to 128. Occasional comparative runs used yet higher resolutions. The scope of these simulations was severely restricted by available computer resources and the magnetic field could not be included. For this reason, an expansion valid for small precession rates similar to the one used by Hollerbach & Kerswell (1995) has been adopted. This expansion conveniently separates the influence of different terms and allows more insight than the direct simulation.

For the Earth, $\alpha = 23.5^\circ$ and $\Omega \approx -10^{-7}$. It is therefore natural to consider equations (1), (2) for small Ω and \mathbf{u} and to obtain at first order the velocity \mathbf{u}_1 , magnetic field \mathbf{b}_1 and reduced pressure Φ_1 :

$$\frac{\partial}{\partial t} \mathbf{u}_1 + 2\hat{\mathbf{z}} \times \mathbf{u}_1 = -\nabla \Phi_1 + Ek \nabla^2 \mathbf{u}_1 - (\boldsymbol{\Omega} \times \hat{\mathbf{z}}) \times \mathbf{r} + (\nabla \times \mathbf{b}_1) \times \mathbf{B}_d, \quad (9a)$$

$$\frac{\partial}{\partial t} \mathbf{b}_1 + (\mathbf{u}_1 \cdot \nabla) \mathbf{B}_d - (\mathbf{B}_d \cdot \nabla) \mathbf{u}_1 = \frac{Ek}{Pm} \nabla^2 \mathbf{b}_1. \quad (9b)$$

Having computed \mathbf{u}_1 and \mathbf{b}_1 it is possible to proceed to the next order and find

nonlinear responses \mathbf{u}_0 and \mathbf{b}_0 :

$$\frac{\partial}{\partial t} \mathbf{u}_0 + (\nabla \times \mathbf{u}_1 + 2\boldsymbol{\Omega}) \times \mathbf{u}_1 + 2\hat{\mathbf{z}} \times \mathbf{u}_0 = -\nabla\Phi_0 + Ek\nabla^2 \mathbf{u}_0 + (\nabla \times \mathbf{b}_1) \times \mathbf{b}_1 + (\nabla \times \mathbf{b}_0) \times \mathbf{B}_d, \quad (10a)$$

$$\frac{\partial}{\partial t} \mathbf{b}_0 + \nabla \times (\mathbf{b}_1 \times \mathbf{u}_1 + \mathbf{B}_d \times \mathbf{u}_0) = \frac{Ek}{Pm} \nabla^2 \mathbf{b}_0. \quad (10b)$$

At the boundaries, \mathbf{u}_1 and \mathbf{u}_0 satisfy no-slip conditions, and \mathbf{b}_1 and \mathbf{b}_0 match external potential fields; \mathbf{u}_1 , \mathbf{b}_1 , \mathbf{u}_0 and \mathbf{b}_0 are all solenoidal. The forcing term $-(\boldsymbol{\Omega} \times \hat{\mathbf{z}}) \times \mathbf{r}$ is purely $m = 1$. The indices are justified by the fact that \mathbf{u}_1 and \mathbf{b}_1 then also have only $m = 1$ components, whereas \mathbf{u}_0 and \mathbf{b}_0 have non-vanishing amplitudes at $m = 0$. There are also contributions to \mathbf{u}_0 and \mathbf{b}_0 at $m = 1$ and 2, but these have not been investigated in any detail in the present work because experimental pictures reveal only axisymmetric shear layers.

It is a straightforward matter to extend the discretization described above for the original equations (1), (2) to the perturbation equations (9), (10). The resolutions used in the computations are included in table 1.

Time integration has been continued for at least 250 revolutions of the shell for the direct simulations. Using the expansion for low precession rates, runs lasted 1000 revolutions for the non-magnetic cases and 40 revolutions at the highest Elsasser number. All runs eventually led to flows whose sole time dependence consists in a global rotation following the movement of $\hat{\boldsymbol{\Omega}}$ in the mantle frame. Only these final states will be considered. Transient oscillations seemed to always disappear and are certainly less than 10^{-3} in fractional amplitude should they persist. Equations (1), (2) are invariant under the transformation $\mathbf{r} \rightarrow -\mathbf{r}$, $\mathbf{u} \rightarrow -\mathbf{u}$. All solutions which have been obtained are antisymmetric with respect to inversion at the origin. This symmetry was always recovered after random perturbations had been added and time integration continued.

3. Direct simulations

This section begins with a discussion of theoretical ideas which will help to organize the presentation of the numerical results. Only flows in the absence of a magnetic field will be considered. Theoretical work is generally easier in a frame of reference rotating about the axis of precession with angular velocity $\boldsymbol{\Omega}$ in which the axes of precession and rotation of the shell are stationary. In this frame, Cartesian basis vectors $\hat{\mathbf{i}}$, $\hat{\mathbf{j}}$ and $\hat{\mathbf{k}}$ are chosen such that $\boldsymbol{\Omega} = \Omega\hat{\mathbf{k}}$ and $\hat{\mathbf{z}} = \sin\alpha\hat{\mathbf{i}} + \cos\alpha\hat{\mathbf{k}}$. The boundary conditions for \mathbf{u} in this frame are $\mathbf{u} = \hat{\mathbf{z}} \times \mathbf{r}$ at $r = r_i, r_o$ and the equation of motion becomes

$$\frac{\partial}{\partial t} \mathbf{u} + (\nabla \times \mathbf{u}) \times \mathbf{u} + 2\boldsymbol{\Omega} \times \mathbf{u} = -\nabla\Phi + Ek\nabla^2 \mathbf{u}. \quad (11)$$

A solution to this equation is a solid-body rotation $\boldsymbol{\omega}_F \times \mathbf{r}$ with $\boldsymbol{\omega}_F$ determined by the interaction of the interior flow with the Ekman layers which form in order to satisfy the boundary conditions. A simple idea used by Vanyo & Likins (1972) consists in subsuming the viscous effects in a frictional force per unit area proportional to $(\hat{\mathbf{z}} - \boldsymbol{\omega}_F) \times \mathbf{r}$ acting at the boundaries. In dimensional units, the prefactor is given by $\rho\nu/h$, where h stands for the thickness of the boundary layers which will have to be chosen empirically. Using this approximation and operating with $\int dV \mathbf{r} \times$ on (11) yields

$$\frac{d}{dt} \boldsymbol{\omega}_F = \boldsymbol{\omega}_F \times \boldsymbol{\Omega} + \gamma(\hat{\mathbf{z}} - \boldsymbol{\omega}_F), \quad \gamma = 5 \frac{\nu}{\omega d h} \frac{r_o^4 + r_i^4}{r_o^5 - r_i^5}. \quad (12)$$

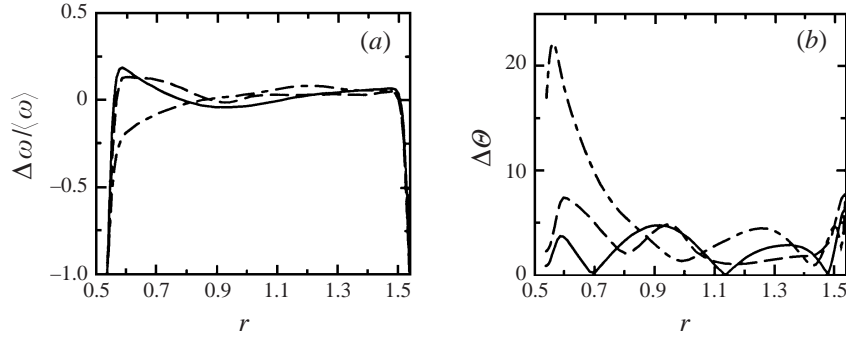


FIGURE 1. Deviations from a solid-body rotation as a function of radius r ($r_i = 0.35/0.65, r_o = 1/0.65$): (a) magnitude of the local deviation $\Delta\omega(r)$ of the angular velocity from the average, divided by $\langle\omega\rangle = |\langle\omega\rangle|$; (b) angle $\Delta\theta$ between $\omega(r)$ and $\langle\omega\rangle$ in degrees. $\alpha = 23.5^\circ$ for all three curves. The other parameters are $Ek = 10^{-4}, \Omega = -10^{-3}$ (solid line), $Ek = 10^{-4}, \Omega = -0.2$ (dot-dashed line), and $Ek = 10^{-5}, \Omega = -10^{-3}$ (dashed line).

In the stationary state, ω_F is given by

$$\omega_F = \frac{\gamma^2}{\gamma^2 + \Omega^2} \sin \alpha \hat{\mathbf{i}} - \frac{\gamma\Omega}{\gamma^2 + \Omega^2} \sin \alpha \hat{\mathbf{j}} + \cos \alpha \hat{\mathbf{k}}. \quad (13)$$

Independently of the choice of h one finds for the stationary state $\omega_F \cdot \hat{\mathbf{z}} = \omega_F^2$ and $(\omega_F \cdot \hat{\mathbf{j}})\Omega < 0$. The latter inequality shows that viewed in an inertial frame, the axis of the fluid lags behind the axis of the shell in the precessional motion. At infinitesimal Ω , $\omega_F - \hat{\mathbf{z}}$ is orthogonal to Ω and $\hat{\mathbf{z}}$. As $|\Omega|$ is increased, ω_F gradually aligns with $\hat{\mathbf{k}}$.

A calculation by Busse (1968) determined ω_F for a spheroid from an expansion in Ekman and Rossby numbers. This calculation is considerably more involved and leads qualitatively to the same conclusions as the above model, but free of any adjustable parameter like h . In particular, ω_F is determined by

$$\frac{\omega_F}{\omega_F^2} = \hat{\mathbf{z}} + \frac{A\hat{\mathbf{z}} \times (\Omega \times \hat{\mathbf{z}}) + B(\hat{\mathbf{z}} \times \Omega)}{A^2 + B^2}, \quad (14)$$

with $A = 0.259(Ek/\omega_F)^{1/2}/r_o + \Omega \cdot \hat{\mathbf{z}}$ and $B = 2.62(Ek\omega_F)^{1/2}/r_o$ for a spherical boundary of radius r_o (see also Roberts & Stewartson 1965). The z -component of (14) reproduces the equation $\omega_F \cdot \hat{\mathbf{z}} = \omega_F^2$ already obtained above. Equation (14) strictly speaking holds for a full sphere. However, equation (12) shows that the torque exerted by the inner core on the fluid in a shell with $r_i/r_o = 0.35$ is only 2% of the total frictional torque, so that (14) can be reasonably applied to the present situation.

We now turn to a comparison with numerical results. Three series of runs have been performed: (i) $Ek = 10^{-4}, \alpha = 23.5^\circ$ with $-10^{-3} \geq \Omega \geq -0.2$, (ii) $Ek = 10^{-4}, \alpha = 90^\circ$ with $-10^{-3} \geq \Omega \geq -10^{-2}$ and (iii) $Ek = 10^{-5}, \alpha = 23.5^\circ$ with $\Omega = -10^{-3}$ and $\Omega = -3 \times 10^{-3}$. Precession is thus retrograde in all cases. Two points are included ($Ek = 10^{-5}, \Omega = -3 \times 10^{-3}$ and $Ek = 10^{-4}, \alpha = 90^\circ, \Omega = -10^{-2}$) for which equation (1) has been time stepped without the term $(\nabla \times \mathbf{u}) \times \mathbf{u}$. This term is unimportant for a comparison with the above theory, as could be verified by comparing results obtained with and without the nonlinear term for other parameter sets. However, it is not possible to judge the stability of the computed flows in these two cases.

Figure 1 quantifies the deviations from a solid-body rotation. For this purpose, the rotation vector $\omega(r)$ of the fluid on a spherical surface with radius r is computed in

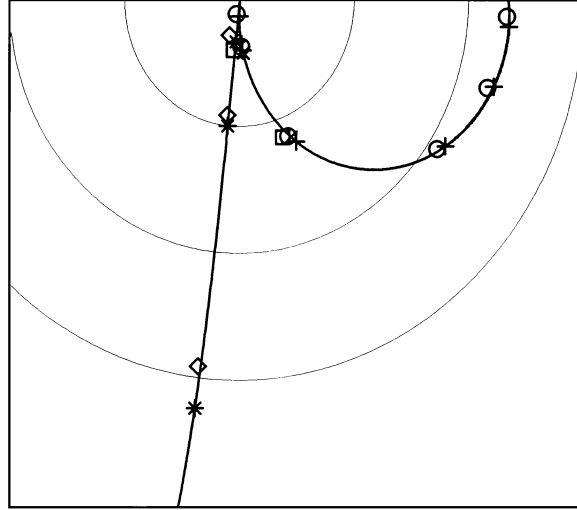


FIGURE 2. Polar plot showing the orientation of the average rotation of the fluid in a reference frame in which the axes of precession and rotation of the shell are stationary. The thin circles are located at 10° , 20° and 30° from the north pole. The thick lines show the locus of the directions of the rotation axis of the fluid predicted by (14) for $\alpha = 90^\circ$ (left-hand line) and $\alpha = 23.5^\circ$ (right-hand line), the latter ending at the top right of the figure at the position of the precession axis. ‘Retrograde’ corresponds to ‘clockwise’ in this figure. The symbols indicate $Ek = 10^{-4}$, $\alpha = 23.5^\circ$ (circles), $Ek = 10^{-5}$, $\alpha = 23.5^\circ$ (squares) and $Ek = 10^{-4}$, $\alpha = 90^\circ$ (diamonds). The values of Ω can be deduced from figure 3 where more data for the same runs are shown; the points close to the pole are for small $|\Omega|$. Near to every data point obtained from direct simulation is another symbol showing the direction calculated with (14) for the same parameter set: crosses belong to circles, \times to squares and stars to diamonds.

the mantle system:

$$\boldsymbol{\omega}(r) = -2\text{Re}\{W_1^1(r)\}\hat{\mathbf{x}} + 2\text{Im}\{W_1^1(r)\}\hat{\mathbf{y}} + W_1^0(r)\hat{\mathbf{z}}. \quad (15)$$

$\text{Re}\{\}$ and $\text{Im}\{\}$ denote the real and imaginary parts of the quantity in curly brackets. An average rotation is then defined by $\langle \boldsymbol{\omega} \rangle = \frac{1}{V} \int \boldsymbol{\omega}(r) dV$, where V is the volume of the shell. Figure 1(a) shows the deviation of the rotation rate $\Delta\omega = |\boldsymbol{\omega}(r)| - |\langle \boldsymbol{\omega} \rangle|$, figure 1(b) shows the variation of the angle between local and average rotation as a function of radius, $\cos \Delta\theta = \boldsymbol{\omega}(r) \cdot \langle \boldsymbol{\omega} \rangle (|\boldsymbol{\omega}(r)| |\langle \boldsymbol{\omega} \rangle|)^{-1}$. Even well outside the viscous layers, $\Delta\omega/|\langle \boldsymbol{\omega} \rangle|$ always exceeds 8% at some radius. The angle $\Delta\theta$ reaches 5° in all cases. Reducing the Ekman number barely reduces these deviations.

We can next transform $\langle \boldsymbol{\omega} \rangle$ into the coordinate system spanned by $\hat{\mathbf{i}}$, $\hat{\mathbf{j}}$ and $\hat{\mathbf{k}}$ and compare $\langle \boldsymbol{\omega} \rangle + \hat{\mathbf{z}}$ with $\boldsymbol{\omega}_F$. Figure 2 shows a polar diagram in which the directions of $\langle \boldsymbol{\omega} \rangle + \hat{\mathbf{z}}$ and $\boldsymbol{\omega}_F$ are given. This plot is the analogue of figure 3 in Vanyo *et al.* (1995) in which the position of the rotation axis of the fluid is deduced from the motion of tracer particles and from the orientation of shear layers. A quantitative comparison is not possible because the experiment was at lower Ek and in an ellipsoidal container. The locus of the directions of $\langle \boldsymbol{\omega} \rangle + \hat{\mathbf{z}}$ when varying Ω depends on α but not on Ek according to (14). This is verified well by the numerical results. Differences between the predicted and computed directions are of the order of the deviations $\Delta\theta$ within which a rotation vector can be defined from the numerical data.

Figure 3 compares the kinetic energy of the flow in the mantle frame with the predicted value $\frac{1}{2} \int (\boldsymbol{\omega}_F - \hat{\mathbf{z}})^2 dV$. The agreement is fair and the fractional error would

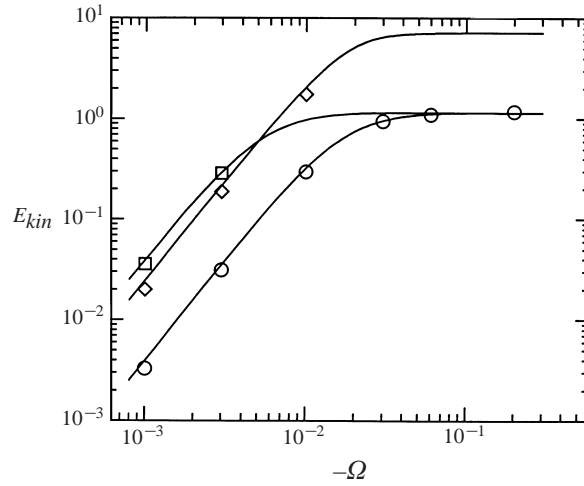


FIGURE 3. Kinetic energy E_{kin} of the flow in the mantle frame as a function of the (retrograde) precession rate Ω . The symbols indicate $Ek = 10^{-4}$, $\alpha = 23.5^\circ$ (circles), $Ek = 10^{-5}$, $\alpha = 23.5^\circ$ (squares) and $Ek = 10^{-4}$, $\alpha = 90^\circ$ (diamonds). The solid lines show the kinetic energies deduced from (14).

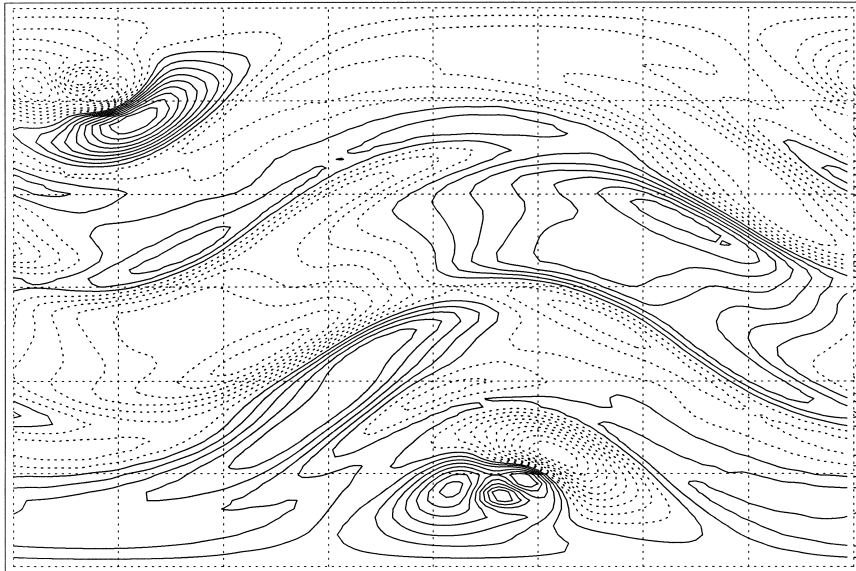


FIGURE 4. Cylindrical projection of contour lines of the radial component of vorticity at mid-shell after the solid-body rotation $\langle \boldsymbol{\omega} \rangle \times \mathbf{r}$ has been subtracted. $Ek = 10^{-4}$, $\alpha = 23.5^\circ$ and $\Omega = -6 \times 10^{-2}$. At the time at which the snapshot is taken, the precession axis lies at colatitude $\theta = 23.5^\circ$ and longitude $\varphi = -130^\circ$ ($\varphi = 0$ is in the middle of the figure). The axis of rotation of the fluid points at $\theta = 23^\circ$ and $\varphi = -147^\circ$ ($\theta = 111^\circ$ and $\varphi = -147^\circ$ for the fluid rotation relative to the shell).

appear even smaller in the $\hat{i}, \hat{j}, \hat{k}$ frame because most of the rotational energy is subtracted out in transforming to the mantle frame, where deviations from solid-body rotation are emphasized. The agreement also improves with decreasing Ek .

It is natural to inquire what the structures of the flow superimposed on the solid-body rotation look like. It is known from the experiments that shear layers occur

| Ek | Pm | El | n_r | L | $\frac{E_{1,tor} \times 10^{-4}}{(\Omega \sin \alpha)^2}$ | $\frac{E_{1,pol} \times 10^{-2}}{(\Omega \sin \alpha)^2}$ | $\frac{E_{b,tor}}{(\Omega \sin \alpha)^2}$ | $\frac{E_{b,pol}}{(\Omega \sin \alpha)^2}$ | $\frac{E_{0,tor} \times 10^{-7}}{(\Omega \sin \alpha)^4}$ | $\frac{E_{0,pol} \times 10^{-6}}{(\Omega \sin \alpha)^4}$ |
|--------------------|------|------|-------|-----|---|---|--|--|---|---|
| 10^{-4} | – | 0 | 65 | 64 | 1.99 | 1.92 | – | – | 4.12 | 3.67 |
| 10^{-5} | – | 0 | 129 | 128 | 14.0 | 5.50 | – | – | 172 | 192 |
| 3×10^{-6} | – | 0 | 129 | 256 | 25.9 | 5.86 | – | – | 490 | 600 |
| 10^{-4} | 0.1 | 0.1 | 65 | 64 | 1.99 | 1.83 | 1.83 | 6.59 | 4.05 | 4.22 |
| 10^{-4} | 0.1 | 1 | 65 | 64 | 1.54 | 1.38 | 17.3 | 45.5 | 2.61 | 2.53 |
| 10^{-4} | 0.1 | 10 | 129 | 64 | 0.417 | 0.795 | 31.2 | 112 | 0.31 | 0.44 |
| 10^{-4} | 1 | 0.1 | 65 | 64 | 1.91 | 1.81 | 1.89 | 3.37 | 3.69 | 3.82 |
| 10^{-4} | 1 | 1 | 65 | 64 | 1.80 | 1.77 | 9.15 | 18.2 | 3.12 | 5.10 |
| 10^{-4} | 1 | 10 | 129 | 64 | 1.10 | 1.41 | 42.9 | 83.0 | 1.35 | 2.74 |
| 10^{-5} | 1 | 0.1 | 65 | 128 | 13.6 | 5.4 | 3.88 | 7.04 | 159 | 222 |
| 10^{-5} | 1 | 1 | 129 | 128 | 19.1 | 8.48 | 37.0 | 60.4 | 353 | 910 |

TABLE 1. Kinetic energies E_1 and E_0 contained in the $m = 1$ and $m = 0$ modes, respectively, as well as the energy E_b contained in the $m = 1$ modes of the magnetic field for solutions of equations (9), (10) at Ekman number Ek , Prandtl number Pm and Elsasser number El computed with resolutions of n_r radial collocation points and spherical harmonics of degree up to L . Energies for toroidal and poloidal components are given separately and indicated by the subscripts *pol* and *tor*. All energies are rescaled with the appropriate power of the driving force $\Omega \sin \alpha$. Errors are less than 5% on all quantities. The energy in $m = 2$ modes is less than a third of E_0 except at $Ek = 3 \times 10^{-6}$ where it is about one half the energy contained in the $m = 0$ components.

which are axisymmetric about the rotation axis of the fluid. In order to render such layers visible in the numerical data, figure 4 shows a cylindrical projection of the spherical surface at mid-shell on which the radial component of vorticity is plotted after the solid-body contribution has been removed. While a very weak shear layer roughly symmetric about the rotation axis of the fluid appears at about 60° from that axis (such a layer takes a wavy form in the cylindrical projection), the picture is dominated by non-axisymmetric features. This trend should reverse at lower Ek (see §5).

None of the flow structures showed any sign of instability in the parameter range investigated. It is seen from figure 3 that the flow is unlikely to become unstable at yet larger $|\Omega|$ at $Ek = 10^{-4}$, $\alpha = 23.5^\circ$ because the kinetic energy has saturated. Reducing Ek does not increase that saturation energy but increases the Reynolds number. The numerical simulation of precession-driven flows which do become unstable will be a future challenge. Only the basic flow is treated in this paper. Instead of dissecting its structure with cumbersome three-dimensional visualization, it was found more illuminating to follow the perturbation approach as reported in the next two sections.

4. Non-axisymmetric components of magnetohydrodynamic flows

This section deals with the solution of equations (9a,b) in the presence of an imposed magnetic dipole field. The parameter range covered in this study is $10^{-4} \geq Ek \geq 3 \times 10^{-6}$, $0 \leq El \leq 10$, $0.1 \leq Pm \leq 1$. Table 1 lists the parameters actually used.

4.1. Flow structures

Figure 5 shows flow structures after the solid-body rotation $\langle \boldsymbol{\omega} \rangle \times \mathbf{r}$ as defined in the previous section has been subtracted. The remaining components of the meridional flow reach their maximum in the meridional plane containing $\langle \boldsymbol{\omega} \rangle$, whereas the azimuthal component becomes maximum in the meridional plane perpendicular to

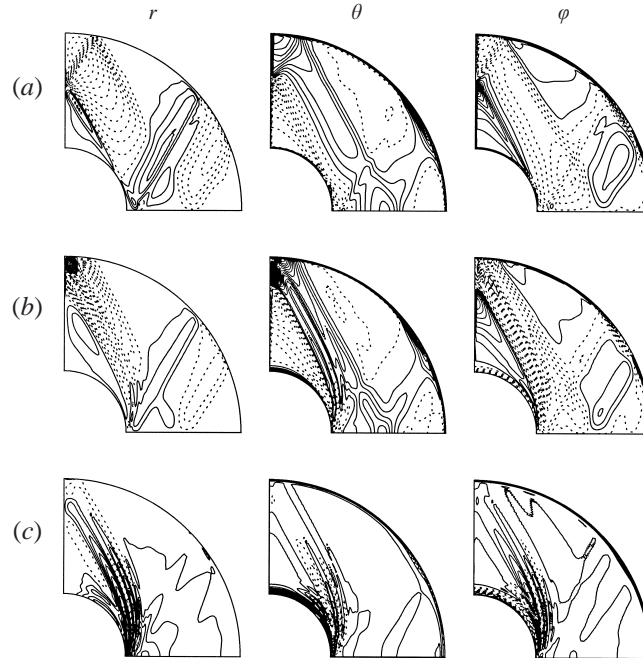


FIGURE 5. Visualization of \mathbf{u}_1 and \mathbf{b}_1 (equations (9a,b)) in meridional planes. Solid (dashed) contours indicate positive (negative) values. (a) $Ek = 10^{-5}$, no magnetic field is applied; (b,c) $Ek = 10^{-5}$, $Pm = 1$, $El = 1$; (a,b) show (from left to right) the r -, θ - and φ -components of \mathbf{u}_1 , (c) shows from left to right the r -, θ - and φ -components of \mathbf{b}_1 . u_{1r} , $u_{1\theta}$, b_{1r} and $b_{1\theta}$ are given in the plane containing $\langle \boldsymbol{\omega} \rangle$, which points to the right. $u_{1\varphi}$ and $b_{1\varphi}$ are shown in a plane such that $\langle \boldsymbol{\omega} \rangle$ points out of the figure.

the previous one. These planes have been chosen for the cuts shown in figure 5 because the shear zones are most visible there. In the non-magnetic case (figure 5a), the critical latitudes which generate shear layers inclined at 30° with respect to the axis of rotation are clearly visible. As could be expected, these circulations are very similar to the spin-over mode obtained by Hollerbach & Kerswell (1995).

Figure 5(b) shows the influence of a magnetic field at $El = 1$. The most important effect is visible at the inner core, where the point from which shear layers erupt moves towards the equator, but the characteristic angle of inclination for interior shear layers remains the same. The shear zones tend to split into several layers emanating from the equatorial region. This is most clearly seen from figure 5(c) where the magnetic field is shown. Due to the $(\mathbf{B}_d \cdot \nabla) \mathbf{u}_1$ term in (9b), the magnetic field probes the derivatives of the velocity field and is particularly sensitive to additional structure; \mathbf{b}_1 is mostly confined to shear layers and spreads with increasing Ek and decreasing Pm .

Figure 6 shows the dependence on Ek , El and Pm . The radial velocity component gives a sufficiently general impression of the flow. At $Ek = 10^{-4}$, all features are of course more smeared out than at $Ek = 10^{-5}$. At the highest El one observes that the flow structures tend to align with the z -axis. The lower Pm accentuates the effect of the magnetic field: in figure 6, the structure at $Pm = 0.1$, $El = 0.1$ superficially looks like the flow at $Pm = 1$, $El = 1$, and the pictures for $Pm = 0.1$, $El = 1$ and $Pm = 1$, $El = 10$ resemble each other, too.

The remainder of this subsection attempts to interpret some of these results in terms of a simple model. Imposing a magnetic field of strength $(El Ek / Pm)^{1/2}$ on

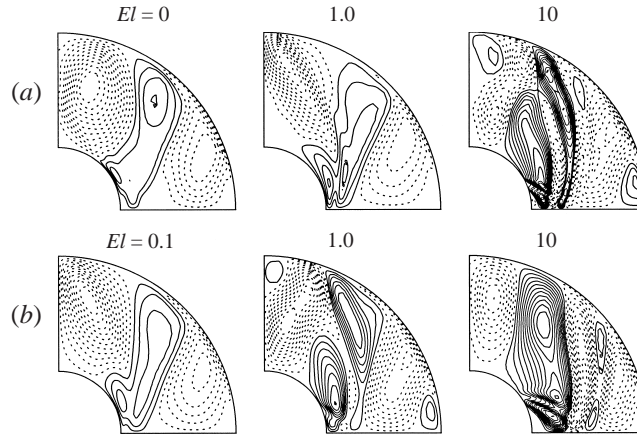


FIGURE 6. Radial component of \mathbf{u}_1 in the meridional plane containing $\langle \omega \rangle$. All plots are for $Ek = 10^{-4}$, (a) $Pm = 1$, (b) 0.1, and El as indicated.

a flow of typical velocity v_0 varying on length and time scales of order 1 yields an induced magnetic field of order of magnitude $(El Ek/Pm)^{1/2}v_0$ if the diffusion term in the induction equation is small. The magnetic term in the Navier–Stokes equation is therefore of the order of $El Ek/Pm v_0$ which is negligible compared with the Coriolis force in all cases of interest. The form of the primary flow, i.e. the solid-body rotation, is thus hardly affected by the magnetic field.

These estimates are different inside the shear layers. It looks paradoxical at first that the boundary layer eruptions and their associated shear layers are displaced towards the equator, a region of higher magnetic field strength. In order to gain some understanding of the dynamics, consider a flow in which the interior motion is assumed to be a solid-body rotation $\boldsymbol{\omega} \times \mathbf{r}$ with $\boldsymbol{\omega} = \sin t \hat{\mathbf{x}} + \cos t \hat{\mathbf{y}}$, and the flow near the boundaries is determined by the boundary layer versions of (9a,b). Let us focus on the case $Pm \ll 1$, relevant for the Earth. Anticipating boundary layer thicknesses of $Ek^{1/2}$ or less, the magnetic diffusion time across the layers will be Pm or less, i.e. small compared to 1. The time derivative term in the induction equation can thus be neglected as the magnetic field can quickly adjust to the variation of the velocity field occurring on the time scale $O(1)$. The equations for the boundary layer quantities $v_\theta, v_\phi, \tilde{b}_\theta, \tilde{b}_\phi$ become with the usual approximations

$$\frac{\partial}{\partial t} \begin{pmatrix} v_\theta \\ v_\phi \end{pmatrix} + 2 \cos \theta \begin{pmatrix} -v_\phi \\ v_\theta \end{pmatrix} = Ek \frac{\partial^2}{\partial z'^2} \begin{pmatrix} v_\theta \\ v_\phi \end{pmatrix} + \hat{\mathbf{n}} \cdot \mathbf{B}_d \frac{\partial}{\partial z'} \begin{pmatrix} \tilde{b}_\theta \\ \tilde{b}_\phi \end{pmatrix}, \quad (16a)$$

$$-\hat{\mathbf{n}} \cdot \mathbf{B}_d \frac{\partial}{\partial z'} \begin{pmatrix} v_\theta \\ v_\phi \end{pmatrix} = \frac{Ek}{Pm} \frac{\partial^2}{\partial z'^2} \begin{pmatrix} \tilde{b}_\theta \\ \tilde{b}_\phi \end{pmatrix}, \quad (16b)$$

where z' denotes distance from the boundary along the normal vector $\hat{\mathbf{n}}$ pointing into the fluid. Equation (16b) can be integrated over z' with the boundary condition that all quantities approach 0 as z' tends towards infinity; \tilde{b}_θ and \tilde{b}_ϕ may then be eliminated from (16a) to yield

$$\frac{\partial}{\partial t} \begin{pmatrix} v_\theta \\ v_\phi \end{pmatrix} + 2 \cos \theta \begin{pmatrix} -v_\phi \\ v_\theta \end{pmatrix} = \left(Ek \frac{\partial^2}{\partial z'^2} - \frac{Pm}{Ek} (\hat{\mathbf{n}} \cdot \mathbf{B}_d)^2 \right) \begin{pmatrix} v_\theta \\ v_\phi \end{pmatrix}. \quad (17)$$

Note that only the normal component of \mathbf{B}_d enters, which acts like an additional dissipation. Equation (17) needs to be solved for (v_θ, v_ϕ) with a time dependence in e^{it}

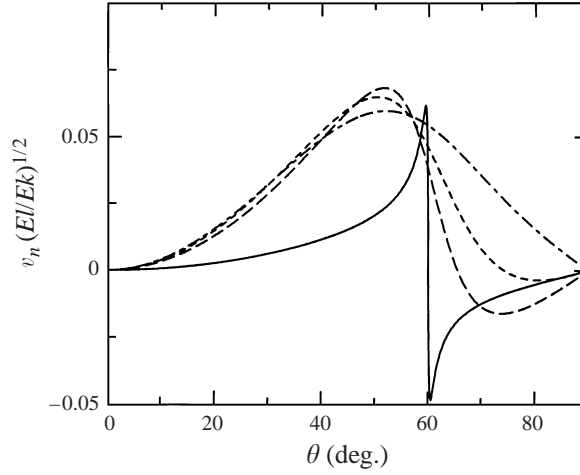


FIGURE 7. The normal component of velocity v_n at the edge of the boundary layer at the inner core computed according to (21) at $\varphi + t = \frac{1}{2}\pi$ and multiplied with $(El/Ek)^{1/2}$ for convenience, as a function of colatitude θ in degrees for $El = 10^{-4}$ (solid line), 3×10^{-3} (long dashed), 5×10^{-3} (short dashed) and 10^{-2} (dot dashed).

and subject to the boundary conditions

$$v_\theta = -R \operatorname{Re}\{e^{i(\varphi+t)}\}, \quad v_\varphi = -R \cos \theta \operatorname{Re}\{ie^{i(\varphi+t)}\} \quad \text{for } z' = 0, \quad (18a)$$

$$v_\theta = v_\varphi = 0 \quad \text{for } z' \rightarrow \infty, \quad (18b)$$

where R denotes the radius of the boundary under consideration. The solution to this problem is

$$v_\theta = -\frac{1}{2}R[(1 - \cos \theta)\operatorname{Re}\{e^{-\alpha_+\zeta}e^{i(\varphi+t)}\} + (1 + \cos \theta)\operatorname{Re}\{e^{-\alpha_-\zeta}e^{i(\varphi+t)}\}], \quad (19a)$$

$$v_\varphi = -\frac{1}{2}R[(1 - \cos \theta)\operatorname{Im}\{e^{-\alpha_+\zeta}e^{i(\varphi+t)}\} - (1 + \cos \theta)\operatorname{Im}\{e^{-\alpha_-\zeta}e^{i(\varphi+t)}\}], \quad (19b)$$

with $\zeta = Ek^{-1/2}z'$ and

$$\alpha_\pm = \left(i(1 \pm 2 \cos \theta) + \frac{Pm}{Ek}(\hat{\mathbf{n}} \cdot \mathbf{B}_d)^2 \right)^{1/2} = \left(i(1 \pm 2 \cos \theta) + 4El \left(\frac{r_i r_o}{R^2} \right)^3 \cos^2 \theta \right)^{1/2}, \quad (20)$$

the root with positive real part being understood. Here, one can check that the approximations made above are consistent. The boundary layer thicknesses are indeed of the order $Ek^{-1/2}$ at $El = 0$ and decrease with increasing El (which explains why higher El requires higher radial resolution in numerical computations, see table 1). The normal velocity v_n is obtained from the equation of continuity. At the surface of the boundary layer ($\zeta \rightarrow \infty$), v_n is given by

$$v_n(\zeta = \infty) = Ek^{1/2} \frac{1 - \cos 2\theta}{2 \sin \theta} \operatorname{Re} \left\{ \left(\frac{1}{\alpha_+} - \frac{1}{\alpha_-} \right) e^{i(\varphi+t)} \right\}. \quad (21)$$

The solution (19a,b) is in agreement with numerical results near the inner boundary for z' up to about $2Ek^{-1/2}$ for $El = 0$. At the outer boundary, impinging shear layers originating from the inner core complicate the picture. As v_θ and v_φ become small for large ζ , they are eventually dominated by the interior corrections to the solid-body rotation $\langle \boldsymbol{\omega} \rangle \times \mathbf{r}$ at large enough ζ . The structure of the flow at z' a few multiples

of $Ek^{-1/2}$ can thus be quite different from the boundary layer flow. Figure 7 shows for instance $v_n(\zeta = \infty)$ as a function of θ at $\varphi + t = \frac{1}{2}\pi$ for various El at the inner boundary. It is seen that a change of sign occurs at around $\theta = 60^\circ$ for small El which turns into a singularity for $El = 0$. However, as figure 6 shows, the radial velocity just outside the boundary layer has an extremum (rather than a root) at this colatitude in this particular meridional plane for $Ek = 10^{-4}$. This is not true any more at the inner core for $Ek = 10^{-5}$ (figure 5).

So far there is no rigorous connection between the boundary layer flow and an internal shear layer. However, the change of sign in $v_n(\zeta = \infty)$ signals a special latitude and is certainly indicative of large shear. We will adopt that change of sign as a marker for the latitude at which internal shear layers are spawned. Full visualization of the boundary layer solution also leads to the conclusion that the flow pattern in the boundary layer is moving towards the equator with increasing El . The origin of internal shear layers should therefore shift towards the equator, too, simply because that origin follows the entire boundary layer flow pattern. This shift towards the equator occurs in the numerical simulation only at a higher El than predicted by (21), the discrepancy being larger for larger Pm . But remember that $Pm \ll 1$ was assumed in the derivation of (21). According to (20) the same shift also occurs at the outer boundary but requires an El larger by a factor $(r_o/r_i)^6$ to produce the same effect. This is again compatible with the numerical data. Note that the entire derivation has been independent of the boundary conditions on \mathbf{b} in the limit $Pm \ll 1$. The same behaviour is thus expected for a conducting inner core at small Pm .

The region around $\theta = 60^\circ$ remains distinguished at high El because a maximum of $v_n(\zeta = \infty)$ occurs there. This might be related to the shear zones which reappear for $El = 10$ at the inner core at $\theta = 60^\circ$. To complete the analysis one would have to calculate the corrections to the interior flow and determine the structure of the internal shear zones analytically. This appears to be quite difficult (even in the non-magnetic case) especially near the equator.

4.2. Energies

Table 1 gives further quantitative data obtained from the solutions of equations (9a,b). The poloidal and toroidal contributions to the kinetic and magnetic energies (integrated over the volume of the shell) are listed separately. It is seen that reducing the Ekman number increases all energies. This is expected since the impact of the diffusion terms is then lowered. At the same time, the ratio of poloidal to toroidal kinetic energies decreases due to less efficient Ekman pumping. An increase of El can either increase or decrease the kinetic energy. A stronger magnetic field has a damping effect on one hand, on the other hand it decreases the boundary layer thickness (as can be deduced from (20)) and leads to a stronger coupling between the fluid and the boundary, hence to more efficient energy transfer.

5. Axisymmetric components of magnetohydrodynamic flows

This section deals with the solutions of equations (10a,b). Figure 8 shows the structure of \mathbf{u}_0 for various parameter sets. A solid-body contribution has again been subtracted for clarity, which was in all cases a retrograde rotation about the z -axis. One recognizes features familiar from experiments (Malkus 1968) or theory (Busse 1968): moving radially inwards starting from the equatorial region at the outer boundary, one crosses successively zones of retrograde, prograde and again retrograde velocity, which are superimposed on the general retrograde circulation. The shear layers in that

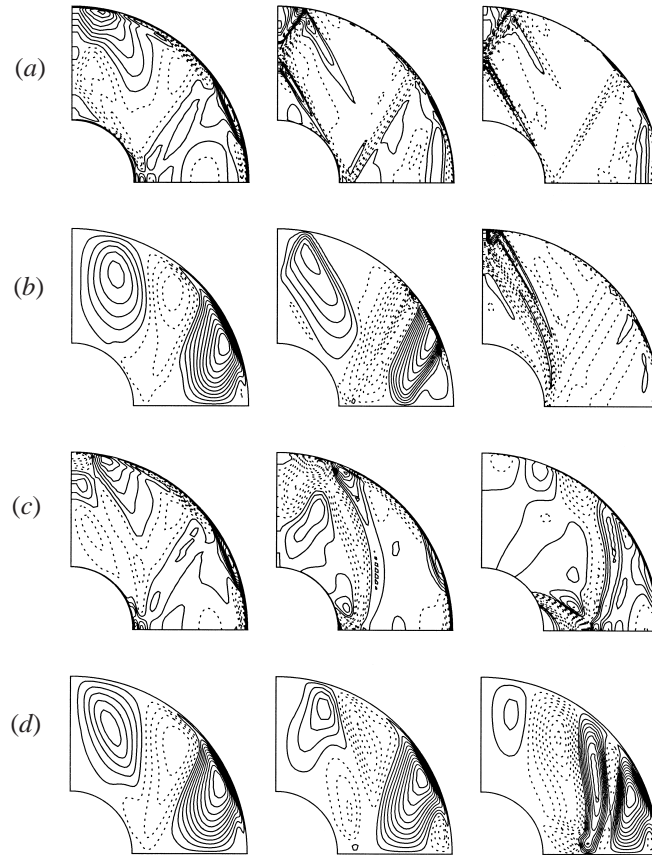


FIGURE 8. Meridional circulation and zonal component of \mathbf{u}_0 (equation (10a)). Continuous lines indicate clockwise rotation in the meridional circulation. The zonal flow is shown for $Ek = 10^{-4}$, $El = 0$ (a, left), $Ek = 10^{-5}$, $El = 0$ (a, middle), $Ek = 3 \times 10^{-6}$, $El = 0$ (a, right) and $Ek = 10^{-5}$, $Pm = 1$, $El = 1$ (b, right). All the plots in (c) are for $Ek = 10^{-4}$, $Pm = 0.1$ but with $El = 0.1$ (left), 1 (middle) and 10 (right). The remaining panels show meridional circulations for the same parameters as for the panels directly above: $Ek = 10^{-4}$, $El = 0$ (b, left), $Ek = 10^{-5}$, $El = 0$ (b, middle); $Ek = 10^{-4}$, $Pm = 0.1$ for all plots in (d) with $El = 0.1$ (left), 1 (middle) and 10 (right).

region are however not exactly located at the distance $r_o \cos 30^\circ$ from the z -axis, at which they would connect the critical latitudes at the outer boundary. The strongest shear layers are those originating from the inner boundary. Figure 4 gives a hint of the existence of such shear layers in a much more nonlinear regime in which the perturbation approach is not directly applicable.

The non-magnetic results can also be compared with the figures given by Hollerbach & Kerswell (1995) who solved (10a) for $\Omega = 0$ and zero magnetic field using for \mathbf{u}_1 the velocity of the decaying spin-over mode. The forcing term has then a time dependence $e^{-2\lambda t}$ where λ is the decay rate of the spin-over mode. Hollerbach & Kerswell looked for the particular solution of (10a) which also decays like $e^{-2\lambda t}$. However, this solution could not be obtained by time integration because the homogeneous part of (10a) has solutions decaying more slowly which dominate the time-stepped solution at any instant if time integration is started from the steady-state flow as initial condition. There are striking differences between the solution of Hollerbach & Kerswell (1995) and the steady-state flows of figure 8 as far as the φ -component is concerned (where

the nested cylindrical shear layers seen in the decaying solution have essentially disappeared), but the meridional circulations are surprisingly similar.

When the magnetic field is added, the structures in \mathbf{u}_0 follow the same general trend as those in \mathbf{u}_1 by which they are driven: the characteristic angle of 30° loses its prominence; the z -axis becomes a distinguished direction in the bulk of the shell where the flow structures appear to become independent of the inner core.

The poloidal and toroidal energies of \mathbf{u}_0 are also given in table 1. The meridional component is considerably weaker than the φ -component. At equal $\Omega \sin \alpha$, the ratio E_0/E_1 rapidly increases with decreasing Ek . Axisymmetric shear layers should therefore become more visible than in figure 4 with decreasing Ek .

6. Conclusion and outlook

Experiments attempting to model the Earth's outer liquid core have shown that shear layers appear in precessing flows which become unstable at large enough precession rates. It has been surmised that the resulting flow may lead to a dynamo effect. The present work investigates what happens to these shear layers in the presence of an inner core and a magnetic dipole field. For a ratio of inner to outer radius of 0.35, the inner core has a negligible effect on the primary flow. The torque exerted by the inner core on the fluid is so small that the orientation and magnitude of the rotation vector of the fluid can be predicted with a formula originally derived for a full spheroid. The structure of the flow superimposed on the primary solid-body rotation is dominated by shear layers originating from the inner core. An applied magnetic dipole field modifies the boundary layers and also the position and structure of the internal shear layers. With increasing magnetic field strength, the characteristic angle of 30° loses its significance. The results on magnetohydrodynamic flows have been obtained at the lowest order for small precession rates. It should be noted that in this limit in the absence of a magnetic field, critical latitudes are always at 60° to the axis of the shell, whereas in a full theory they occur at 60° to the rotation axis of the fluid. Similarly, the orientation of shear layers in the magnetohydrodynamic flows is likely to be modified at higher precession rates. The limit of slow precession is of importance in the geophysical context, however.

A direct comparison with existing experiments is not possible at present because none has included an inner core. Nested axisymmetric shear layers which dominate the flow in full spheroids give way to axisymmetric conical shear layers in most of the volume of the spherical shell used in the computations. Only comparatively weak axisymmetric shear layers have been observed in the direct simulations because the Ekman number was still much larger than those encountered in experiments. Malkus (1971) gives an approximate criterion for the onset of instability of the shear layers in his experiments, which is $(1 - \omega_F^2)Ek^{-1/2} \geq 2$ in the notation of §3. The direct simulations in §3 reached $(1 - \omega_F^2)Ek^{-1/2} \approx 10$, yet showed no sign of instability. This might be due to the difference in flow structures, to uncertainties in the determination of ω_F which needs to be accurate to a few percent, or to too high an Ekman number for Malkus' criterion to be valid. It will be the subject of future work to numerically reach situations in which the flow becomes unstable and to investigate the dynamics of a precession-driven dynamo. The computations with an imposed magnetic field of §§4 and 5 lead one to expect different regimes for weak and strong field dynamos because different shear layers dominate at different Elsasser and magnetic Prandtl numbers.

The author wishes to acknowledge F. H. Busse for helpful discussions.

REFERENCES

- BONDI, H. & LYTTLETON, R. A. 1953 On the dynamical theory of the rotation of the Earth: the effect of precession on the motion of the liquid core. *Proc. Camb. Phil. Soc.* **49**, 498.
- BULLARD, E. C. 1949 The magnetic field within the Earth. *Proc. R. Soc. Lond. A* **197**, 433.
- BUSSE, F. H. 1968 Steady fluid flow in a precessing spheroidal shell. *J. Fluid Mech.* **33**, 739.
- GANS, R. F. 1970 On hydromagnetic precession in a cylinder. *J. Fluid Mech.* **45**, 111.
- HOLLERBACH, R. & KERSWELL, R. R. 1995 Oscillatory internal shear layers in rotating and precessing flows. *J. Fluid Mech.* **298**, 327.
- KERSWELL, R. R. 1995 On the internal shear layers spawned by the critical regions in oscillatory Ekman boundary layers. *J. Fluid Mech.* **298**, 311.
- KERSWELL, R. R. 1996 Upper bounds on the energy dissipation in turbulent precession. *J. Fluid Mech.* **321**, 335.
- MALKUS, W. V. R. 1968 Precession of the Earth as the cause of geomagnetism. *Science* **169**, 259.
- MALKUS, W. V. R. 1971 Do precessional torques cause geomagnetism? In *Mathematical Problems in the Geophysical Sciences, Lectures in Applied Mathematics*, vol. 14 (ed. W. H. Reid), p. 207. Am. Math. Soc.
- ROBERTS, P. H. & STEWARTSON, K. 1965 On the motion of a liquid in a spheroidal cavity of a precessing rigid body. II. *Proc. Camb. Phil. Soc.* **61**, 279.
- STEWARTSON, K. & ROBERTS, P. H. 1963 On the motion of a liquid in a spheroidal cavity of a precessing rigid body. *J. Fluid Mech.* **17**, 1.
- TILGNER, A. 1996 High-Rayleigh-number convection in spherical shells. *Phys. Rev. E* **53**, 4847.
- TILGNER, A. 1997 A kinematic dynamo with a small scale velocity field. *Phys. Lett. A* **226**, 75.
- TILGNER, A. 1999 Spectral methods for the simulation of incompressible flows in spherical shells. *Intl J. Numer. Meth. Fluids* (in press).
- TILGNER, A. & BUSSE, F. H. 1997 Finite-amplitude convection in rotating spherical fluid shells. *J. Fluid Mech.* **332**, 359.
- VANYO, J. P. & LIKINS, P. W. 1972 Rigid-body approximations to turbulent motion in a liquid-filled, precessing, spherical cavity. *Trans. ASME: J. Appl. Mech.* **39**, 18.
- VANYO, J. P., WILDE, P., CARDIN, P. & OLSON, P. 1995 Experiments on precessing flows in the Earth's liquid core. *Geophys. J. Intl* **121**, 136.